Aerodynamic interference between rotors, fuselage, wing and control surfaces of a VTOL UAV

António Reis

antoniofreis98@tecnico.ulisboa.pt

Instituto Superior Técnico, Universidade de Lisboa, Portugal

June 2022

Abstract

This project aims at studying the aerodynamic interference between the rotors, wings, fuselage and control surfaces of a Vertical Take-Off and Landing (VTOL) Unmanned Aerial Vehicle (UAV), developed by Beyond Vision, while, at the same time, assessing the most suitable models to simulate the flow behaviour at different flight stages, through means of Conputational Fluid Dynamics (CFD) calculations. Simulations were performed resorting to Reynolds Averaged Navier-Stokes (RANS) analysis, employing the $K - \omega$ SST turbulence model, characterized by a cruise Mach number of $M = 0.088$, a rotor tip Mach number of $M_{tip} = 0.32$, and a cruise Reynolds number of $Re \approx 3 \times 10^5$. To model the rotors, the Multiple Reference Frame (MRF), Sliding Mesh and Overset Mesh models were considered. A mesh independence study was performed on the rotor, and the results were verified and validated with performance data provided by the manufacturer, and experimental data from Milluzzo et al. (2020)[1]. The MRF model was deemed the most suitable one, according to the required computational cost and the accuracy of the results obtained. During cruise, it was verified that the presence of the VTOL structures, while having the rotor blades parallel with the flow, resulted in increased drag, and decreasing C_L/C_D from 10.45 to 7.28, while worsening the wing's aerodynamic coefficients at the same time. It was observed that the rotor position across the wing had negligible impact on performance, but its orientation relative to the flow did. C_L/C_D was reduced to 6.82 when the rotors were perpendicular to the flow. In vertical flight it was observed that the rotors and airframe interacted mutually, resulting in worse performance, and that having the rotors far from the fuselage reduces rear rotor interference with the tail. In transition flight is was concluded that the MRF method was not suitable for that application, performing simply a qualitative analysis of the flow.

Keywords: Unmanned Aerial Vehicle (UAV), Computational Fluid Dynamics (CFD), Vertical Take-Off and Landing (VTOL), Aerodynamic Interference

1. Introduction

The last decade has been marked by a drastic increase in usage of Unmanned Aerial Vehicles (UAV) both in recreational and commercial environments, adding to their initial use in military applications. Recently, different UAV's capable of Vertical Take-Off and Landing (VTOL), while keeping the conventional fixed-wing, horizontal, flight have been sprouting in the market, as they combine the VTOL and manoeuvrability capabilities of rotorcraft, with the long range and efficiency of conventional fixed-wing aircraft.

A multitude of new studies utilizing different CFD methods have appeared, ranging from simulating newer and older aircraft in hover flight, employing the Overset Mesh model [2] [3], to tilt-rotor and tilt-wing configurations in transition flight employing different methods such as using Overset Meshes, Multiple Reference Frame (MRF) and Actuator Disk modelling based on Blade Element Momentum Theory (BEMT) [4] [5] [6].

There are different, well studied, solutions for VTOL flight, each one with its advantages and disadvantages. The most commonly used in VTOL aircraft are: tilt-rotors, in which the rotors tilt in order to produce thrust in vertical or horizontal flight; tilt-wings, which are similar but the wing, or a section of it, tilts together with the rotor; and the Separate Lift and Thrust (SLT) in which vertical and horizontal flight are governed by two different powertrains. Other possible configurations are tail-sitters or multicopters.

From these configurations, tilt-rotors and tilt-wings have the best performance in long range missions, multicopters have the best performance in vertical flight, as stated, and STL UAVs prove to be a good compromise between both. [7].

This project focuses on the aerodynamic study

of the beVTOne, a SLT UAV developed by Beyond Vision, by means of CFD calculations. Possible models to simulate rotor motion are identified and their suitability for the intended purpose is evaluated. By the end of this work, one should have an understanding of the aerodynamic interactions at play between its different components and have conclusions regarding the best suiting model for this study.

2. Project Background
2.1. beVTOne Overview
This work focuses on the study of the beVTOne VTOL UAV developed by Beyond Vision. The beVTOne is an electric, multi purpose, UAV, specifically designed for commercial uses such has agriculture, powerline inspection or any other advanced monitoring application. Furthermore, it is dimensioned according to NATO requirements, meaning that it can also be employed in military applications. Its layout consists of a traditional quad configuration for VTOL flight and a pusher at the rear for cruise flight, commonly known as a Separate Lift and Thrust configuration.

A typical flight mission profile is displayed in figure 1, being composed by vertical take-off and climb up to a height of $60m$, followed by transition to conventional flight and a further climb up to the cruise height of $120m$. Then, cruise flight follows, when the UAV is performing its assigned mission. Finally, the UAV transitions once again to vertical flight, descending axially and landing.
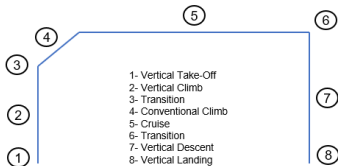

Figure 1: Typical mission profile.

With a Maximum Take-Off Weight (MTOW) of $10kg$, its payload can consist of cameras and other sensors or cargo of up to $2kg$. The technical specifications are presented in table 1.

Table 1: beVTOne technical specifications

Characteristics:	Value:
Height	500 mm
Length	1200 mm
Wingspan (b)	2560 mm
Mean Chord ($\bar{c}$)	150 mm
Wing Area (S)	0.384 m^2
Flight Height	120 m
Cruise Speed	30 m/s
Cruise Range	240 km

2.2. Mathematical Models
In order to simulate fluid flow, ANSYS Fluent [8] utilizes the Finite Volume Method (FVM) to solve the Navier-Stokes Equations [9], which govern the behaviour of fluid flow. The FVM discretizes the spatial domain into separate elements, which together constitute a mesh, and solves discretized forms of the equations presented in this chapter for each individual element.

When using the FVM, the way to accurately capture turbulent flow characteristics is to have very small spatial discretization, which can capture the smallest eddies, with a suitably small time discretization to capture temporal effects. This process is called Direct Numerical Simulation (DNS) but it requires a high number of elements (proportional to Re^3), which translates to unfeasibly demanding computational power requirements. The answer to this is to use the Reynolds-Averaged Navier-Stokes (RANS) equations, where the flow variables coming fro the Navier-Stokes equations are substituted by their decomposition into mean value components and a fluctuating components, and then the original are averaged [10]. The resulting averaged equations are given by

$$\nabla \cdot \left(\rho \bar{\mathbf{U}} \right) = 0 \qquad (1)$$

and

$$\frac{\partial}{\partial t} \left(\rho \bar{\mathbf{U}} \right) + \nabla \cdot \left(\rho \overline{\mathbf{U}\mathbf{U}} \right) = -\nabla \bar{p} +$$
$$+ \left[\nabla \cdot \left(\bar{\bar{\boldsymbol{\tau}}} - \rho \overline{\mathbf{U}'\mathbf{U}'} \right) \right] + \rho \bar{\mathbf{g}} + \bar{\mathbf{F}}, \quad (2)$$

where t represents time, $\bar{U}$ is the mean velocity vector, $\bar{p}$ is the mean static pressure field, $\bar{\bar{\tau}}$ is the mean shear stress tensor, ρ is the fluid density, $\bar{g}$ is the mean gravitational acceleration vector, $\bar{F}$ is the mean body force vector and, finally $\boldsymbol{\tau}^R = -\rho \overline{U'U'}$ represents the Reynods Stress Tensor. This tensor introduces six new turbulent variables which must be solved to close the system of equations. To do so, turbulence models are used. Two turbulence models widely used in aerospace applications were considered in this work, the $k - \omega$ Shear Stress Transport (SST) model, and the Spalart-Allmaras model.

The $k - \omega$ SST model closes the RANS system of equations with two transport equations for turbulent kinetic energy, k, and other for the turbulence frequency, ω. It combines the robustness of the $k - \varepsilon$ model in the fully turbulent region far from the walls with the accuracy of Wilcox's $k - \omega$ model in the near-wall regions. This model has a wide range of applicability in external aerodynamics studies, and has shown accurate results at modelling the flow in null and adverse pressure gradients, highly important characteristic while study-

ing airfoils. [11] The Spalart-Allmaras model introduces one transport equation to model the kinematic eddy viscosity and close the RANS equations. This model was specifically developed and tuned for aerospace applications. It was shown to give good performance when evaluating boundary layers with adverse pressure gradients, however, it lacks calibration for general industrial applications and produces relatively larger errors for free shear flows, as is the case of a massive separation occurrence, free wakes with pressure gradients or free vortices. [12]

A final model is required to simulate rotor motion. Three different methods were considered in this work, the MRF, the Sliding Mesh and the Overset Mesh. In the MRF model, the fluid domain is divided into at least two zones, one corresponding to the background, stationary domain, and an inner moving zone around the rotating body, where a moving reference frame is defined. Then, the governing flow equations are solved relative to the respective zone. The governing flow equations for a steadily rotating frame are [8]:

$$\frac{\partial \rho}{\partial t} + \nabla \cdot \rho \mathbf{U_r} = 0 \qquad (3)$$

as the conservation of mass,

$$\frac{\partial}{\partial t}\left(\rho \mathbf{U}\right) + \nabla \cdot \left(\rho \mathbf{U_r} \mathbf{U}\right) + \rho \left[\boldsymbol{\omega} \times \left(\mathbf{U} - \mathbf{V_t}\right)\right] =$$
$$= -\nabla p + \nabla \cdot \bar{\tau} + \mathbf{F} \quad (4)$$

as the conservation of momentum equation.

This model, however, does not capture the unsteady interaction between stationary and moving parts. Despite this, it can provide a reasonable approximation of the flow in applications where the interaction between moving and rotating parts is relatively weak and the flow is relatively uncomplicated at the interfaces between different zones.

In the Sliding Mesh formulation the domain is divided similarly to the MRF formulation, however, the desired motion of the moving body is prescribed to the mesh elements inside the moving zone. The integral form of the conservation equation for a general variable, ϕ, on a given control volume, V, whose boundary is moving is written as

$$\frac{d}{dt}\int_V \rho\phi dV + \int_{\partial V} \rho\phi\left(\mathbf{U} - \mathbf{U}_g\right)\cdot d\mathbf{A} =$$
$$= \int_{\partial V} \Gamma\nabla\phi\cdot d\mathbf{A} + \int_V S_\phi dV, \quad (5)$$

where $\mathbf{U}_g$ is the velocity of the moving mesh, $\mathbf{A}$ is the area vector normal to the control volume surface, Γ is the diffusion coefficient, S_ϕ is the source term of ϕ, if there's any, and ∂V represents the boundary of the control volume, V. This equation applies to all model equations, such as momentum, energy, turbulence, etc. When using this method the zones must be defined such that the prescribed motion allows them to keep contact with each other along the non-conformal interface, that is, both zones "slide" along the interface boundary [8].

In the Overset Mesh formulation, overset interfaces connect cell zones by interpolating cell data in overlapping regions. The model needs to be constituted of at least two cell zones, a background mesh which represents the broader domain, and a component mesh around the body of interest. This body can either be stationary or moving[13]. When the simulation is initialized, the necessary connectivity between the different meshes is established. The cells where the flow equations are solved are referred to as solve cells, receptor cells receive data in a mesh interpolated from another mesh and donor cells are the cells where the receptors get their data from. In this approach, the governing equations are the same as the ones employed with the Sliding Mesh model. One important aspect of overset meshes is that, when mesh motion is present, the interface connectivity must be re-calculated in each time step, which introduces an increase in computational time required. While using the Sliding Mesh or the Overset Mesh formulations, selecting the appropriate time step size is of utmost importance for better accuracy and stability. The ideal time step should be chosen such that the relative mesh motion does not exceed the length of the smallest cell in the overset overlap region, in a given time step.

3. Implementation
3.1. Geometry Setup
The initial UAV configuration, shown in figure 2, modeled using the Computer Aided Design (CAD) software SolidWorks was provided by Beyond Vision.
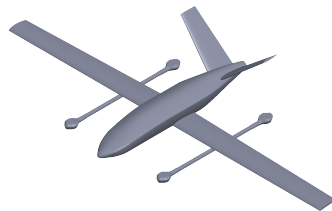

Figure 2: Initial beVTOne geometry provided by Beyond Vision.

Before discretizing the domain, one first repairs ill-defined geometry features by the CAD software. This is done by using ANSYS Spaceclaim CAD soft-

3

ware [14], which provides a series of geometry repair tools targeted at Computer Aided Engineering (CAE) applications.

Lastly, before exporting the geometries to the meshing software, the fluid domains are generated and volumes are created around areas of interest to later be used in ANSYS Meshing for local refinement. Only half of the domain was modelled due to its symmetry characteristics.

3.2. Mesh Generation

Before solving the RANS equations, the fluid domain must be discretized, and, to do so, the element type must be chosen, between hexaedral, tetrahedral or polyhedral. According to Sosnowski (2018) [15], polyhedral meshes have a level of numerical diffusion comparable to that of hexahedral meshes, which have the lowest diffusion, and can be easily applied even to very complex geometries. Sosnowski [15] concludes that polyhedral meshes contribute to a higher stability, fewer iterations to achieve a converged solution, and that fewer elements are needed to reach mesh convergence. For the aforementioned reasons, polyhedral meshes were used in this work. To generate the mesh, a tetrahedral mesh was created in ANSYS Meshing [16], exported to ANSYS Fluent, and there converted into a polyhedral mesh.

Having the meshing method decided, a mesh independency study was performed to identify the adequate element sizes such that the influence of the spatial discretization on the solution is minimized, while still keeping an adequate computational size. The sizing of the UAV components was based on guidelines provided by Beyond Vision based on previous studies, while the described mesh studies were performed to the rotors. An initial simulation was performed with a coarse mesh, followed by successive finer meshes. In each simulation variables of interest were monitored and once the variation of these values became negligible, the smallest mesh in this condition was chosen.

The meshes were generated with the sizes from the me studies and inflation layers were created near the walls to accurately capture the developing boundary layers. These layers were defined according to the Fluent Theory Guide [8], having approximately 10 to 15 layers inside the boundary layer and a y^+ below one.

3.3. Simulation Setup

The flow over the UAV is characterized by a cruise Mach number of $M_c = 0.088$ and a Reynolds number of $Re = 3.04 \times 10^5$. On the other hand, the rotor, at its maximum studied rotation speed, has a tip Mach number of $M_{tip} = 0.32$. According to [9], at this Mach number, the change in *rho* due to compressibility effects is of less of 5%. Given that,

and the fact that the high Mach numbers are only present in a small region near the rotor tip, it was decided to use the incompressible solver, together with the pressure-based coupled solver to solve the RANS equations due to the lower computational requirements.

The RANS equations were, therefore, solved for incompressible, flow, together with Menter's $k - \omega$ SST turbulence model, since it has been widely tested and verified in aeronautical applications, coupled with being more stable during the testing phase justified this decision. Coupled with the aforementioned equations, a low y^+ wall treatment was used to accurately describe the boundary layers.

When modelling rotating zones using the MRF model, the steady-state solver was utilized, whereas with Sliding Mesh and Overset Mesh models the transient solver was utilized and a temporal discretization had to be specified. In both cases the time step was chosen with the goal of respecting the Courant-Friedrichs-Lewy condition[17]. Initial studies on the unsteady simulations show that a time step of $\Delta t \approx 2 \times 10^{-6}s$ is required. With such temporal discretization a total of 6550 time steps are required to simulate a full rotation. Since multiple rotations are required to obtain an accurate solution, this number proves to be prohibitively high in this type of engineering application. Furthermore, as later shown the results yielded using the MRF model prove to be accurate enough, thus this model ended up being used throughout the simulations.

In all the cases being studied, the UAV and rotor surfaces were set to the No-slip Wall boundary condition, with the extra detail that in vertical and transition flight the rotor surfaces had to be defined as fixed in the stationary reference frame. The symmetry plane was also set to the equally named boundary condition in all the simulations. In horizontal and transition flight, the upwind, side, top and bottom boundaries were all set as a velocity inlet. There, the flow velocity was specified based on its cruise magnitude of $30m/s$ and aligned with the Z-axis. The free stream turbulent kinetic energy and the turbulence frequency were also defined in this boundary based on Menter's guidelines [11]. In vertical flight the top and all the side boundaries were treated as one Inlet and the bottom boundary as a pressure outlet. In hover, the inlet was assigned a pressure inlet as to allow the air velocity to be fully induced by the rotors, whereas in vertical climb a velocity inlet was assigned, based on the climb velocity with its direction aligned with the Y-axis. The turbulent parameters were defined as previously explained. The final condition to be defined regards the rotor's motion in vertical and

transition flight. In this cases both rotor fluid zones were assigned frame motion, relative to their axes of rotation.

3.4. Verification and Validation

Before proceeding with the full UAV studies, the MRF model was verified and validated against the manufacturer's performance sheets [18]. The resulting flow fields were qualitatively evaluated and a good match is observed with typical flow behaviours. Figure 3 shows the velocity field ate the rotor's mid plane. A typical rotor wake is visible below the rotor plane, including its contraction. Moreover, the induced velocities across the span of the blades the expected behaviour, with low velocities near the hub and increasing velocities as one moves towards the tip, due to increased velocities and higher blade angles of attack. Near the tip, lower velocities are identified, due to tip losses caused by vortex generation.
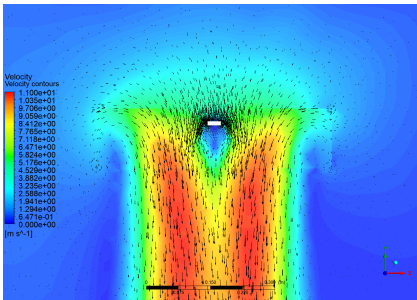

Figure 3: Wake velocity field with rotor operating at 3000RPM

The mass fluxes across the domain's outer boundaries were calculated and yielded a value in the magnitude of 10^{-6}, a negligibly small value, which indicates that mass is being conserved inside the fluid domain. Finally, the resulting performance parameters, namely the thrust coefficient, C_T and power coefficient, $C_P W$, show errors of approximately -5.5% and -7%, respectively, displaying acceptable values of accuracy.

The model was further validated with experimental data from Milluzzo et al. (2020) [1] of rotors operating In Ground Effect (IGE) over inclined surfaces. The ratios of thrust IGE over thrust Out of Ground Effect were compared at different ground inclinations, and the numerical results show a similar trend to the experimental data, with the highest relative error being of -1.3%. The velocity fields, shown in figure 4, with the rotor operating at 4000 RPM over a ground inclination of $10°$, were also compared, and, although they showed different fields due to the different blade geometries, equivalent structures to those present in the experimental results could be identified.
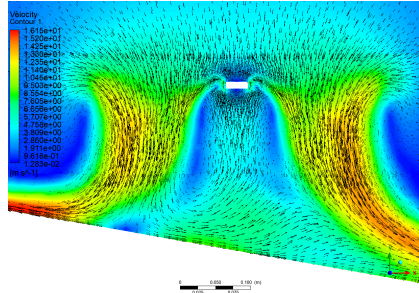

Figure 4: Resulting veocity field from rotor operating at 4000RPM over a ground inclination of $10°$

4. Results

All the simulations were run using a workstation equipped with an 8 Core Intel(R) Xeon(R) W-2245 CPU, clocked at 3.9GHz, with 256 GB of RAM. Simulations were run with 8 solver processes and without GPU acceleration, until the residuals decreased to at least, 10^{-4}, despite that in some cases the turbulent kinetic energy only lowered below 10^{-2} and 10^{-3} in others, and the variables of interest reached a steady value with negligible oscillations. The total number of iterations and time until the solutions converged is shown in table 2.

Table 2: Total number of iterations and computational time until solutions converged.

	Number of iterations	Run time (h)
Conventional UAV (Horizontal)	≈150	≈3
VTOL UAV (Horizontal)	300-400	≈5.5
Conventional UAV (Vertical)	≈200	≈ 3.5
VTOL UAV (Vertical)	8000-10000	≈12
VTOL UAV (Transition)	8000-10000	≈16

4.1. Horizontal Flight

In order to evaluate the aerodynamic interaction between the different UAV components, a baseline must be defined as a mean of comparison. For this purpose, the well studied conventional configuration[19] consisting of the wing, fuselage and tail was chosen. Then, the results obtained from the full VTOL configuration were compared with it. The VTOL geometry was simulated with the rotors located at six different positions across the wing-span with the rotor blades parallel with the flow, and a later simulation was performed with the blades perpendicular to it. From here on this configuration shall be called parallel SLT configuratio.

Analysis of figure 5 shows that the conventional configuration has vortices only behind the fuselage and the wing tip, and when the VTOL structures are installed, they generate meaningful vorticity in their wakes. The original wakes from the conventional geometry appear to be unaffected. From

5

these figures it is expected that a higher rotor/wing interference will be present when the rotors are perpendicular to the flow, since that configuration shows the biggest wake. From here on this configuration is referred to as perpendicular SLT configuration.

The influence of the front rotor wake impinging on the wing is visible on figure 6, where the pressure coefficient, C_p, distributions along the wing chord are displayed for the SLT configurations and compared with the conventional configuration. When the rotors are aligned with the flow, the zone of influence on the wing is narrower and so the C_p plot is evaluated at the rotor plane, however, with the rotors perpendicular to the flow, the influence zone is wide, and the behaviour on each side of the rotor is different since on one side the flow is affected by a rotor blade at a negative incidence angle, and on the other by a positive incidence angle, hence, the C_p plot being evaluated at two planes located at 17.97% and 41.41% of the wing semi-span. The influence of the different blade incidences on the flow streamlines arriving at the wing is shown in figure 7.

Comparing the pressure distribution for the parallel SLT configuration, it can be seen that the peaks only reach values of approximately 0.75 and -1 of maximum and minimum pressure coefficients, respectively, as opposed to the values of approximately 1 and -1.4 obtained in the conventional configuration, and thus, it is expected that less lift is generated in this region. The gap present in the wing's pressure side is caused by the connection between the wing and the boom. The increase in pressure before said connection and the drop right after it occur due to the flow coming to a stop when coming in contact with it, and the small wake left behind it, respectively.

In figure 6 b) one can identify the stronger suction peak present on the wing's lower side, followed by lower pressures on the same side, when compared to the C_p distribution in the conventional configuration. On the suction side it is also visible that throughout the whole top surface suction isn't as strong. Combining this factors, one expects that a lower lift force is generated compared to the conventional configuration. Conversely, in figure 6 c), the opposite is identified. Lower pressures are present on the upper side of the wing, while higher pressures are present at the lower side, and thus one expects lift being increased.

The cause of this behaviour can be identified by analysing figure 7. Analysis of the streamlines shows that the flow meets the blade closer to the fuselage with a positive angle of attack. This blade acts as a wing, deflecting the flow downwards and thus creating downwash. As a consequence of this,

the flow reaches the wing at a lower angle of attack and thus the wing section behind this blade should produce less lift. On the other hand, the air that flows through the blade located away from the fuselage reaches it at a high negative incidence and is, therefore, deflected upwards. This flow, with slight upward velocity, reaches the wing with an increased angle of attack, resulting in higher lift generation behind this blade.

As mentioned above, multiple simulations were performed with the rotors located at $0.2578\frac{b}{2}$, $0.2969\frac{b}{2}$, $0.4141\frac{b}{2}$, $0.5312\frac{b}{2}$, $0.7656\frac{b}{2}$ and $0.8828\frac{b}{2}$, to infer if any meaningful interference was occurring between the rotors and the fuselage, and if that parameter could be modified to increase UAV performance in cruise flight. Figures 8 a) and 8 b) show the variation of the two-dimensional lift, C_l, and drag, C_d, coefficients, respectively, along the wing span for the conventional configuration and the SLT configuration with the rotors located at the aforementioned positions.

As expected, due to three-dimensional effects, lift is maximized near the wing root and decreases as it gets closer to the tip, where it reaches a value of zero. Moreover, these results show that the C_l curve remains almost the same as that of the conventional configuration, and then a dip in C_l is observed at the rotor location with a width comparable to that of the impinging vortex identified in figure 5 b).

The change in C_d along the wing, shown in figure 8 b), is not as clear as with the C_l distribution where a simple dip could be identified, however, by closely examining the curve, one concludes that the relative variation in drag introduced by the rotor presence is similar, no matter the rotor's position. This indicates that it is the same flow structure that is inducing these changes, namely the small variations in the vertical component of the flow velocity due to the rotor vortices, which are not symmetric, since the rotor blades have opposing incidences.

The similar behaviour in lift and drag distributions with varying rotor position translates into almost equal wing C_L and C_D, with wing C_L showing approximately a 2% decrease compared with the conventional configuration and wing C_D showing a lest than 1% increase throughout the different positions. From these results, one concludes that the rotor position along the wing-span does not influence the UAV performance in cruise flight.

Similar plots are generated for the perpendicular SLT configuration and are shown in figure . These plots directly corroborate the predictions made by analysis of figures 6 and 7, where a decrease in C_l is observed at the side of rotor close to the fuselage, and an increase at the side far from the fuselage. The impact on the wing from having the rotors in this orientation is that wing C_L decreases approxi-
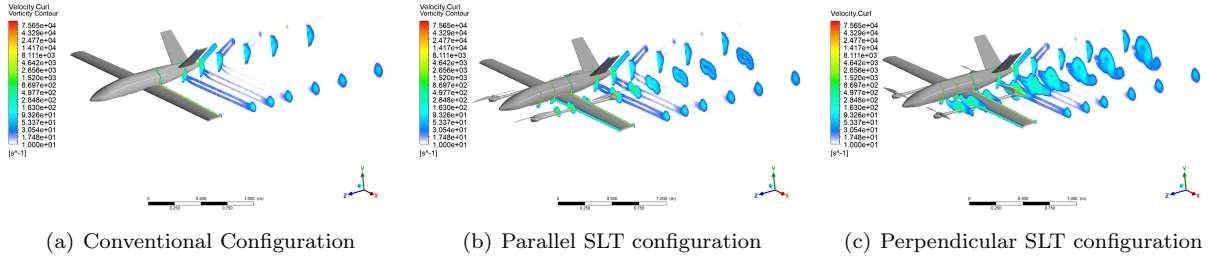
(a) Conventional Configuration (b) Parallel SLT configuration (c) Perpendicular SLT configuration

Figure 5: Visualization of the streamwise vorticity contours.

(a) 29.69% of wing semi-span With rotors alined with the flow

(a) 17.97% of the wing semi-span.

(b) 17.97% of wing semi-span in perpendicular SLT configuration (c) 41.41% of wing semi-span in perpendicular SLT configuration

(b) 41.41% of the wing semi-span.
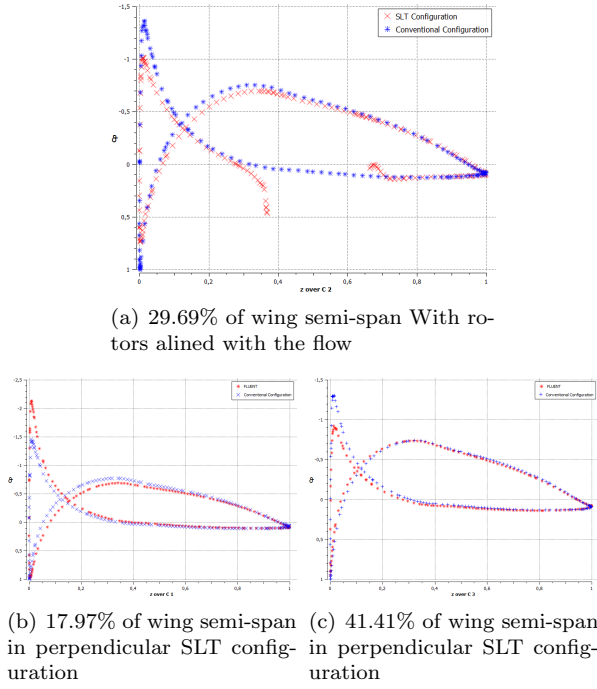
Figure 6: Comparison between C_p distribution in conventional configuration with the parallel SLT configurationa), and the perpendicular SLT configuration, b) and c).

Figure 7: Velocity field visualization in two planes located in the middle of each rotor blade.

mately 5.5% and wing C_D decreases 3.9%.

The total aerodynamic performance coefficients of the UAV in each configuration is show in table 3. From this values on concludes that the VTOL structures create a meaningful decrease in performance in cruise flight, which is mainly attributed to the increase in drag introduced by the presence of said structures. It is shown, however that, even though the performance can't be enhanced by changing the rotor position along the wing, it can be influenced by the orientation of the rotor blades with the flow.

4.2. Vertical Flight

To analyse vertical flight, similar procedures to those in cruise flight were followed. An isolated rotor was simulated in hover and at axial climb speeds
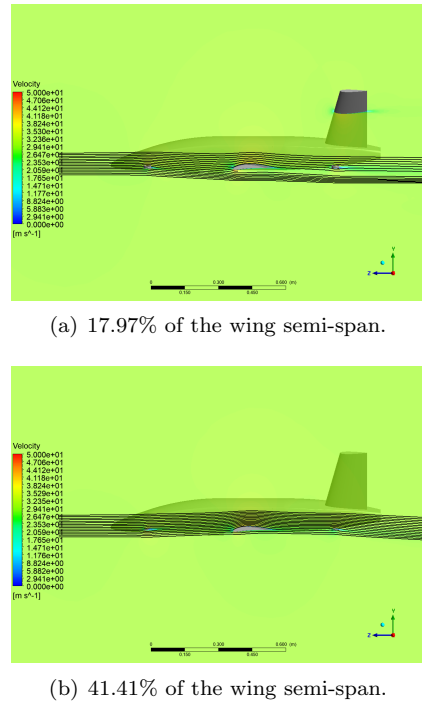
Table 3: Aerodynamic performance coefficients comparison between the three studied configurations.

	Total C_L	Total C_D	$\frac{C_L}{C_D}$
Conventional configuration	0.16497	0.015782	10.45
Original SLT configuration	0.16525	0.022683	7.28
Perpendicular SLT configuration	0.17097	0.025059	6.82

of 0.5, 1. 1.5, 2, 3 and 4m/s, with its rotation speed specified such that the thrust remained constant and that it corresponded to a quarter of the UAV MTOW. The thrust and power coefficient obtained from these simulations were used as the baseline for comparison of rotor performance in the simulations with the full SLT configuration. Similarly, the conventional airframe was simulated at the same climb
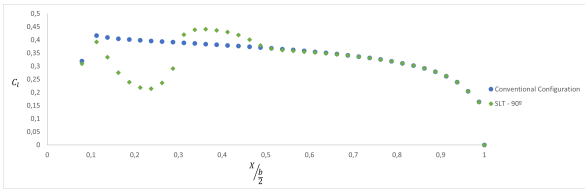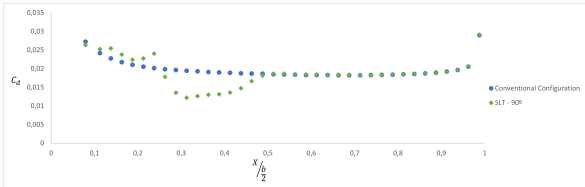
7
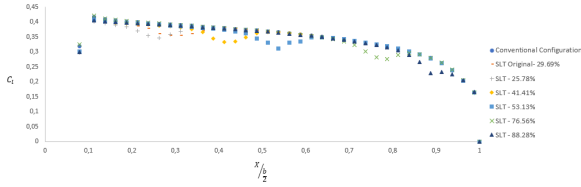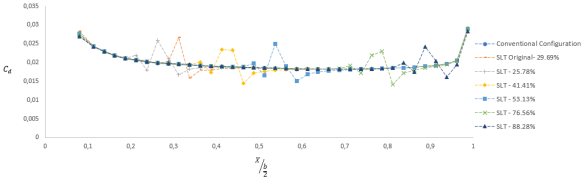
(a) C_l distribution.

(b) C_d distribution.

Figure 8: Two-dimensional lift and drag coefficient distribution along wing semi-span.

(a) C_l distribution.

(b) C_d distribution.

Figure 9: Two-dimensional lift and drag coefficient distribution along wing semi-span in the perpendicular SLT configuration.

speeds so that the downloads on the fuselage, F_f, wing, F_w and tail, F_t could be registered and used as the baseline for comparison with the SLT configuration.

Finally, the same simulations were performed with full SLT configuration. By having defined the aforementioned baselines for comparison, one can more accurately assess the extent to which the loads on the airframe are directly caused by the velocities induced by the rotors and how the variations in rotor performance are caused by direct interference of the airframe.

Figure 10 shows a comparison of the downloads applied on the fuselage, wing and tail, non dimensionalized with the UAV MTOW, represented by W, between the conventional airframe and the full VTOL configuration at the aforementioned climb speeds. It becomes evident that even though the downloads in the fuselage and wing may show very

small oscillations, the tail presents a clear increase which must caused by interaction between the rotors and the tail. In fact, the rear rotor is slightly located below the tail, meaning that such interaction is to be expected. The increase in download at the tail is thus attributed to the local increase in vertical velocity due to rotor's induced velocity.

Conversely, figure 11 shows the comparison between the thrust coefficient in the front and rear rotors in the VTOL configuration, and the isolated rotor. It is seen in hover the front rotor has a very slight decrease in thrust, however the rear rotor shows a palpable variation. This, once again, can be attributed to the interaction between the rear rotor and the tail. The rotor is pulling air and inducing velocity to generate thrust, however, the tail functions has a obstruction which reduces the airflow feeding the rotor, and thus resulting in a thrust penalty. When climb velocity increases, however, this effect gets inverted, and the rear rotor starts generating higher thrusts than its isolated counterpart. An explanation to this effect is that, as axial velocity increases, the vertical component of the velocity vector relative to the rotor blade increases, which results in a reduction of the angle of attack between the flow and the blade, and thus, thrust decreases. To counteract this and keep thrust constant, the rotation speed of the rotor is increased during climb. In this specific case, the same tail that functioned as an obstruction in hover, now shields the rotor from the vertical velocities. Since the rotation speed of the rotor was increased to match higher vertical velocities than those actually present at the rotor, higher thrust is generated.

To reduce this interference, further simulations were performed at a climb speed of 4m/s, with the rotors located at 37.5%, 45.3% and 53.1% of the wing semi-span, and the changes in tail download were assessed. Figure 12 shows those changes, and in can immediately be seen that, as the rotors are moved further away from the tail, the download tends to that of the conventional configuration.

This interaction can be visualized on the velocity fields in the rear rotor plane, shown in figure 13, with rotors located at the original position of $29.7\%\frac{b}{2}$ and at $45.3\%\frac{b}{2}$. The blockage caused by the tail can be clearly identified in figure 13 a), and its effect reduced in figure 13 b).

The global impact of the rotor position on the UAV during vertical flight can be evaluated by the ratio of the required thrust to balance the UAV weight and the downloads, and its MTOW, given by $\frac{T}{W}$. At a climb velocity of $4m/s$, this value can be seen to reduce from 1.112 to 1.092 by moving the rotor from the original position to a position at 45.3% of the wing semi-span, and better improvements would be observed, were the rotors to be

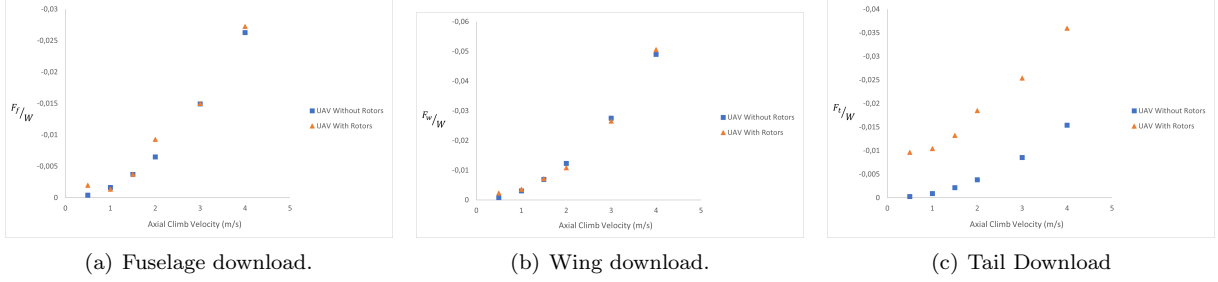(a) Fuselage download. (b) Wing download. (c) Tail Download

Figure 10: Comparison of airframe downloads with and without the effect of the rotors.
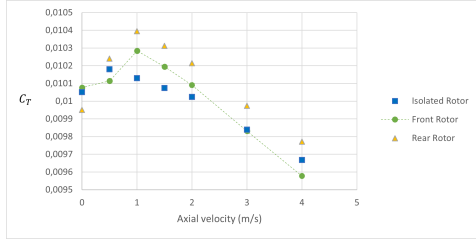

Figure 11: Thrust coefficient comparison between front, rear and isolated rotors at different axial velocities
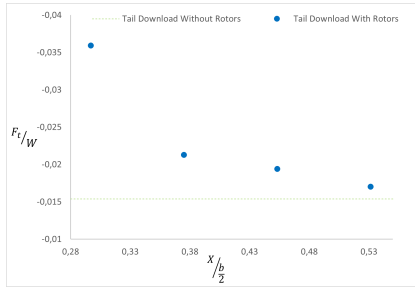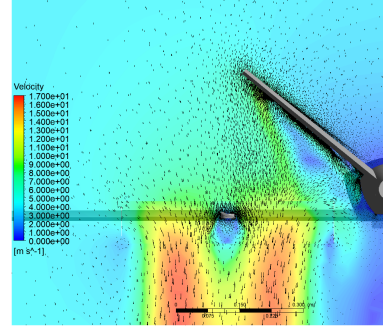

Figure 12: Comparison of tail download at different rotor positions along the wing semi-span.

(a) 29.7% of wing semi-span.

(b) 45.3% of wing semi-span.

Figure 13: Visualization of the flow velocity field on the rear rotor plane, during axial climb, with the rotors located at 29.7% (left) and 45.3% of the wing semi-span.
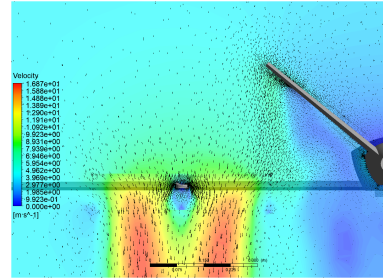
placed further away.

4.3. Transition Flight

The initial goal in this section was to perform simulations with the rotors oriented in the same positions as in subsection 4.1, however, the numerical models/spatial discretization appear to have shown their limitations, has simulations could not meet the predefined convergence criteria, which were later relaxed so that qualitative evaluations could be made to the flow.

The main take-away from these simulations' results is that, during transition flight, the UAV aerodynamics are defined based on the relative intensities of horizontal flight velocity and rotor power. If the UAV is flying at low forward velocities and the rotors are working with at power levels similar to those in vertical flight, then the flow will closely mimic what was seen in subsection 4.2, whereas if

the forward velocity is high and power reduced then it matches better the characteristics of cruise flight. The main interaction that is observed in this flight stage is between the incoming flow and both rotor wakes.

5. Conclusions

A successful prediction of rotor performance, with and without external interference, was achieved by using the MRF method coupled with the $k - \omega$ SST turbulence model.

In cruise flight, important results were obtained regarding the aerodynamic interaction between the conventional configuration and the VTOL components, namely that the rotor position along the wing has no significant impact on the UAV performance, however, the orientation of the rotor blades con-

tributes to a meaningful increase in drag. C_L/C_D was seen to go from 10.45 in the conventional configuration to 7.28 in the parallel SLT configuration and 6.82 in the perpendicular SLT configuration, meaning that, if possible, the rotor should be kept aligned with the flow. For future work the author suggests that a unsteady study be performed to assess the impact on performance when the rotor blades are left to rotate freely based on the aerodynamic loads. Moreover a study on the impact of the VTOL structures on the ailerons and ruddervator could be performed to assess if there are any possible security risks.

In vertical flight, major interference was identified between the rear rotor and the tail. Moreover, it was concluded that the position of the rotors plays a role on the said interference and in climb performance. It was shown that by moving the rotors farther from the tail decreases the downloads on the airframe, which tend to the values obtained when no rotors are present. During climb flight at 4m/s it was seen that by moving the rotors from 29.7% $\frac{b}{2}$ to 45.3% $\frac{b}{2}$, the ration between the required rotor thrust and the UAV MTOW decreases from 1.112 to 1.092. For future work, one could evaluate if deflection on the ruddervators and ailerons can provide further performance increases. Moreover, unsteady calculations can be performed in order to evaluate if any periodic load is present that might bring any risks regarding aeroelastic effects.

Finally, regarding transition flight, even though the MRF method proved effective at modelling the UAV during over and climb, it showed its limitations in transition flight. It is suggested that this flight phase be studied using the Sliding Mesh or the Overset Mesh models.

References

[1] Joseph I. Milluzzo, Aaron Martinez, Scott Drayton, and Scott Davids. Experimental investigation of rotors hovering above inclined surfaces. *Journal of the American Helicopter Society*, 022005:1–12, 2020.

[2] Yong Su Jung, Ju Yeol You, and Oh Joon Kwon. Numerical investigation of prop-rotor and tail-wing aerodynamic interference for a tilt-rotor uav configuration. *Journal of Mechanical Science and Technology*, 28:2609–2617, 2014.

[3] Liang Ye, Ying Zhang, Shuo Yang, Xinglin Zhu, and Jun Dong. Numerical simulation of aerodynamic interaction for a tilt rotor aircraft in helicopter mode. *Chinese Journal of Aeronautics*, 29:843–854, 2016.

[4] Ying Zhang, Liang Ye, and Shuo Yang. Numerical study on flow fields and aerodynamics of tilt rotor aircraft in conversion mode based on embedded grid and actuator model. *Chinese Journal of Aeronautics*, 28:93–102, 2015.

[5] Desmond Adair and Mergen Alimaganbetov. Propeller wing aerodynamic interference for small uavs during vstol 56th israel annual conference on aerospace sciences. pages 0–23, 2016.

[6] Huaping Huang, Guang He, Li Yu, and Xiangke Wang. Numerical analysis on aerodynamic interference of a novel tilt-rotor uav in transition mode. pages 6043–6048, 2020.

[7] Alessandro Bacchini and Enrico Cestino. Electric vtol configurations comparison. *Aerospace*, 6, 3 2019.

[8] *Ansys Fluent Theory Guide*, 2021.

[9] John D Anderson. *Fundamentals of Aerodynamics*. McGraw-Hill Education, 6th edition, 2017.

[10] F. Moukalled, L. Mangani, and M. Darwish. *The Finite Volume Method in Computational Fluid Dynamics*, volume 113. Springer International Publishing, 2016.

[11] F. R. Menter. Two-equation eddy-viscosity turbulence models for engineering applications. *AIAA Journal*, 32:1598–1605, 1994.

[12] P. R. Spalart and S. R. Allmaras. One-equation turbulence model for aerodynamic flows. *Recherche aerospatiale*, pages 5–21, 1994.

[13] *Ansys Fluent User's Guide*, 2021.

[14] *Discovery SpaceClaim*, 2021.

[15] Marcin Sosnowski. The influence of computational domain discretization on cfd results concerning aerodynamics of a vehicle. *Journal of Applied Mathematics and Computational Mechanics*, 17:79–88, 2018.

[16] *Ansys Meshing User's Guide*, 2021.

[17] R. Courant, K. Friedrichs, and H. Lewy. On the partial difference equations of mathematical physics. *IBM Journal of Research and Development*, pages 215–234, 4 (1967) [1928].

[18] 18x8e performance data, 12 2014. Available at https://www.apcprop.com/files/PER3_18x8E.dat.

[19] M.H. Sadraey. *Aircraft Design: A Systems Engineering Approach*. Aerospace Series. John Wiley and Sons, 2012.